ACS APPLIED POLYMER MATERIALS

UNIVERSITY OF BIRMINGHAM

Subscriber access provided by University of Birmingham

Article

Polyvinyl Alcohol Enhances Acetylation of Ascorbic Acid in Superparamagnetic-Graphene Oxide Nanoparticles Ultrasonically Complexed with Acetylsalicylic Acid

Anastasia Tkach, Uladzimir Fiadosenka, Aliaksandr Burko, Hanna V. Bandarenka, Anna Matsukovich, Nina Krekoten, Ljudmila Tabulina, Vladimir Labunov, and Darya Radziuk

ACS Appl. Polym. Mater., **Just Accepted Manuscript** • DOI: 10.1021/acsapm.0c00648 • Publication Date (Web): 15 Jul 2020

Polyvinyl Alcohol Enhances Acetylation of Ascorbic Acid in Superparamagnetic-Graphene Oxide Nanoparticles Ultrasonically Complexed with Acetylsalicylic Acid

*Anastasia Tkach,[1] Uladzimir Fiadosenka,[1] Aliaksandr Burko,[2] Hanna Bandarenka,[2,3] Anna Matsukovich,[4] Nina Krekoten,[5] Ljudmila Tabulina,[1] Vladimir Labunov[1] and Darya Radziuk[1]**

[1]Laboratory of Integrated Micro- and Nanosystems, Belarusian State University of Informatics and Radioelectronics, P. Brovki Str. 6, 220013 Minsk, Republic of Belarus

[2]Laboratory of Applied Plasmonics, Belarusian State University of Informatics and Radioelectronics, P. Brovki Str. 6, 220013 Minsk, Republic of Belarus

[3]Polytechnic School, Arizona State University, 6075 S. Innovation Way, Mesa, AZ, 85212, USA

[4]B.I. Stepanov Institute of Physics, National Academy of Sciences, Nezavisimosti Ave. 68, 220072 Minsk, Republic of Belarus

[5]Scientific-Technical Center "Belmicrosystems", Kazintsa Str. 121 A, 220108 Minsk, Republic of Belarus

KEYWORDS: polymer, graphene, iron oxide, nanoparticle, acetylsalicylic acid.

ABSTRACT

A single step ultrasonic method (20 kHz) is demonstrated for the formation of acetylsalicylic acid-Fe_3O_4-graphene oxide nanocomposites (~ 80 nm) in aqueous solution. The electronic molecular structure of these nanocomposites is stable in acidic or basic aqueous medium. Coating of these nanocomposites with polyvinyl alcohol (PVA) occurs through increased binding with drug, magnetite, Fe(II)-C-O and carbonaceous network of graphene oxide. PVA-coated-acetylsalicylic acid-Fe_3O_4-GO nanocomposites substantially improve acetylation of pristine ascorbic acid than free unmodified drug or uncoated acetylsalicylic acid-Fe_3O_4-GO nanoparticles due to enhanced electron density through the presence of magnetite and graphene oxide, and specific binding of PVA with drug and ascorbic acid.

1. Introduction

Acetylsalicylic acid (ASA) is one of the frequently used nonsteroidal anti-inflammatory drugs (NSAIDs) due to its ability not only to reduce fever and kill the pain, but also to prevent cardiovascular disorders[1] and improve the survival rate after the breast or colon cancer.[2,3] ASA has the unique capacity of acetylating various proteins, hormones, DNA, platelets and hemoglobin, which at least partly explains its wide-ranging pharmacological actions.[4] The pharmacological function of ASA is not completely understood, but can be explained by its inhibition of cyclooxygenase (COX) enzymes that block certain prostaglandins synthesis resulting in reduction of pain, fever and inflammation. ASA forms an ionic bond via its carboxyl or enolic group and acts as one of the strongest inhibitors of COX-1 with much less activity against COX-2, and causes the most damage to the stomach.[5] The recommended dose of ASA for adults to reach the desired analgesic effect is one tablet every 4-6 hours for several days, and to reach the anti-inflammatory effect is about 3 tablets for 4-6 times a day up to 30 tablets daily. A frequency of the ASA administration at such a high dose will unavoidably cause the gastrointestinal tract injury and many other side effects including symptoms such as gas, bloating, and diarrhea, and allergic reactions. Therefore new approaches are necessary for the healthier administration of ASA by reducing its dose and enhancing its pharmaceutical actions.

The pharmacological property of ASA is based on dynamic conformational changes for covalent modification of the COX protein enabling its oxygenation.[6] ASA-treated COX-2 forms polyhydroxylated lipids that exhibit anti-inflammatory activity and can be beneficial for clinical studies. The presence of the carboxylate group affects the charge-charge interaction between ASA and the COX-domain. Conformational changes observed in various NSAID structures have time-dependent inhibition of COX that may occur by more than one mechanism involving

electron or oxygen transfer reactions. Probably for this reason, a large number of NSAIDs can be activated by metal ions resulting in enhanced biological functions including suppression of early cancer relapse and retardation of tumor growth that, in many cases, are inaccessible to pristine NSAIDs.[7] In general, the anti-inflammatory,[8] analgesic,[9] antibacterial[10] and anti-proliferative[11] progression of metal-NSAID complexes rely on their modified chemical structure, i.e. coordination of hydrophilic (carboxylic acid, enols) and lipophilic (aromatic ring, halogen atoms) groups to metal ions. This type of coordination between the metal ion and the NSAID groups determines their interaction with many intracellular components, resulting in the desired cell cure or apoptosis.

Iron metallodrugs are biologically active compounds that constitute a class of approved human or veterinary supplements with improved antitumoral, antimalarial, antifungal and antibacterial activities.[12] At the cellular level the capture of iron ions in biologically useful form occurs through specific complexation with hemoproteins, heme or nonheme enzymes involving electron transfer in oxidation-reduction reactions. The iron ion absorption can be controlled by pH via formation of insoluble ferrous Fe^{3+} and bioavailable ferric Fe^{2+} forms. At low pH, when an iron ion absorption is reduced, the presence of ascorbate and citrate molecular groups can act as weak chelators of metal ions, thereby increasing their bioavailability.[13,14] Complexation of a ferric Fe^{2+} with ASA significantly improves the selective inhibition of COX, stimulating the production and secretion of mucus, increasing mucosal blood flow and promoting epithelial cell proliferation.[15] However, small concentration of such compounds, difficulty in the control of their intact electronic molecular structure and fate *in vivo* substantially limit their application.

This limitation can be overcome by developing new methods in nanomedicine to produce nanoscale compounds with predictable function through the design of their morphology and

electronic molecular structure.[16,17] Morphology and structure of Fe_3O_4 nanoparticles can be controlled by stoichiometry of Fe^{3+} and Fe^{2+} in aqueous medium via classical hydrothermal[18,19] or modified sonochemical[20] routes in conjunction with graphene oxide (GO).[21,22] One of the keys to successful application of such compounds in biomedicine and *in vivo* is the regulation of their toxicity and structure-function property with biomolecules over biocompatible coating. Various hydrophilic polymers (e.g. polyethylene glycol,[23] polyvinyl alcohol,[24] polyaniline,[25] Pluronic F-127,[26] poly (D, L-lactide-co-glycolide),[27] polycyano-acrylate[28]) can be used for such a coating of magnetic nanocomposites reducing aggregation states, improving biocompatibility and stability of morphology, and substantially enhancing their distribution in tissues, cell membrane penetration, intravenous delivery, metabolic clearance and magnetic targeting of nanoparticles *in vivo*. In contrast to nanoparticles, additional parameters such as the number of layers, dimension, and carbon-to-oxygen atomic ratio modulate the toxicity of GO.[29] GO is biodegradable because it can be digested by peroxidases naturally present in cells and its reduced bioaccumulation in cells (tissues) can limit the long-term cytotoxicity.[30] Coating of GO by polyvinyl alcohol (PVA) can significantly reduce the cytotoxicity.[31]

In our study, we develop a new single step ultrasonic method for the complexation of pristine ASA with synthesized Fe_3O_4-GO nanoparticles and coating the final product with PVA in aqueous medium. In this study polymer PVA is chosen for coating because it has a carbon backbone enriched with hydroxyl groups that can substantially enhance the hydrophilicity of produced ASA-Fe_3O_4-GO nanocomposites, improving biocompatibility and dispersion required for biological application. Our work aims at fundamental investigation of acetylation (main function of ASA) of ascorbic acid (AA) as a model system by using ASA- Fe_3O_4-GO nanocomposites coated with PVA and disclose the role of this polymer in this reaction.

2. Experimental Section

Materials and Synthesis. Graphite (~30 μm dispersion) with elemental composition: C (95.0 ± 2.0 atom.%), O (4.0 ± 1.0 atom.%), Ti (0.1 ± 0.0 atom.%), Ca (1.1 ± 0.1 atom.%). H_3PO_4, $KMnO_4$, H_2SO_4, H_2O_2 (60%), HCl (35%), HNO_3 (40%), KOH (44%), NaOH, C_2H_5OH, C_3H_8O, $FeCl_3$ 6 H_2O, $FeCl_2$ 4 H_2O are of higher grade purity 99% being obtained from Belreachim JSC (Republic of Belarus). Deionized water (DI; pH = 5.5, specific conductivity 5 $\mu S \cdot cm^{-1}$) was prepared by using a homemade distillation apparatus (Republic of Belarus). We synthesized graphene oxide (GO) using the improved Hummers method[32] and applied centrifugation (8.59 g) for multiple rinsing, at first, with DI water (pH = 5.5) for a total duration of 90 min and, at second, with a mixture of {DI water : isopropanol} at a volume ratio 1:3 for a total duration of 60 min (more details are in supporting information). The final GO product was obtained after drying at 100°C in the air. Pristine NSAID – acetylsalicylic acid (ASA) (500 mg) was purchased from Belmedpreparaty RUE (Minsk, Republic of Belarus). Fine powder of ASA was produced by grinding of 10 tablets by using agate mortar and pestle. The aqueous solution of ASA was prepared by dissolving a powder of this drug in DI water (pH = 5.5) under continuous stirring at a critical concentration of dissolution at room temperature according to literature.[33] For experiments both NSAID aqueous solutions were filtered through a cellulose membrane filter (red line, the pore size 8-12 nm).

a) Sonochemical formation of graphene oxide-Fe_3O_4 nanoparticles

A homemade horn-type ultrasonic disperser N.4-20 designed by y Cavitation Inc. (Republic of Belarus) and operating in a continuous mode at 20 kHz frequency with the 400 W maximal output power was used for the sonochemical synthesis of nanoparticles. The ultrasonic intensity of this device was calibrated by using a method of calorimetry.[34] Prior to the synthesis of

nanocomposites 0.18 g of GO was exfoliated in 10 mL of DI water (DI) (pH = 5.5) by using ultrasound (10 W/cm^2) for 30 min in ice-cooled vessel. The exfoliated GO was triply rinsed with DI water centrifuged at 7.27 g for 45 min, the supernatant was removed and the precipitant was added by aqueous solution of 44% KOH (pH = 12).

In a vessel of 30 mL H_2O a mixture of {0.86 g $FeCl_2$ + 2.35 g $FeCl_3$} was heated to 80°C in an Ar atmosphere under vigorous stirring for 15 min. Soon after 5 mL 44 % KOH was dropwise added into this heated mixture and the suspension became black. This black solution was heated at 80°C for an additional 30 min under continuous stirring, added by the exfoliated GO (0.14 g of preformed GO was added by 4 mL H_2O and sonicated under stirring until the homogeneous solution was obtained) and sonicated at 18 W/cm^2 for 90 min. This sonochemical synthesis was carried out in a sealed reaction vessel coated by a lid connected to an Ar tube and placed in the ice bath in order to control low temperature. Then the colloidal solution was triply rinsed with DI water at 6.71 g for 30 min and dried at 100°C to obtain a powder. Formed nanocomposites could be easily dispersed in an aqueous solution and collected by an external permanent magnet.

b) Sonochemical coating of graphene oxide-Fe_3O_4 nanoparticles with polyvinyl alcohol

Aqueous solution of PVA was prepared by dissolving 0.022 g of polymer in 10 mL of DI water under stirring in an open air for 30 min. Then it was added by 100 mg of graphene oxide-Fe_3O_4 nanoparticles (powder) and sonicated for 15 min (15 W/cm^2) in an open air in ice-cooled vessel. The final product was triply rinsed by centrifugation at 8.12 g for 15 min and dried at 100°C. This procedure was applied for the coating of preformed Fe_3O_4 nanoparticles.

c) Ultrasonic functionalization of pristine ASA with graphene oxide-Fe_3O_4 and graphene oxide-Fe_3O_4-PVA nanoparticles

Powder of GO-Fe_3O_4 nanoparticles was mixed with the fine powder of pristine ASA at equimolar concentration and ultrasonically treated (18 W/cm^2) in 30 mL of DI water (pH = 5.5) for 5 min in an air in an ice-cooled vessel. Final colloidal suspension was triply rinsed with DI water at 8.12 g for 15 min and dried at 100°C to obtain a powder. Formed nanocomposites could be easily dispersed in aqueous solution and collected by an external permanent magnet.

30 mL of aqueous solution of ASA (1.67 mg/mL) was added by graphene oxide-Fe_3O_4-PVA nanoparticles (10 mg) and sonicated for 5 min (18 W/cm^2) in an open air in an ice-cooled vessel. Final products were triply washed by centrifugation (at 8.12 g) for 15 min and dried at 100°C to obtain a powder. Control experiments were performed by treating each of graphene oxide powder or Fe_3O_4 nanoparticles and the powder of pristine ASA at equimolar concentration with ultrasound (18 W/cm^2) followed by the thorough rinsing with DI water. This procedure was applied for the ultrasonic functionalization of ASA with preformed Fe_3O_4-PVA nanoparticles.

d) Acetylation of pristine ascorbic acid by graphene oxide-Fe_3O_4-ASA and graphene oxide-Fe_3O_4-PVA-ASA nanocomposites

30 mL of aqueous solution of ascorbic acid (1.67 mg/mL) was added by 10 mg of graphene-Fe_3O_4-ASA or graphene-Fe_3O_4-PVA coated-ASA nanocomposites under thermal stirring for 60 min in an air. The temperature of the reaction solution was not allowed to exceed 80°C. After reaction colloidal suspensions were cooled down to room temperature and triply rinsed with DI water by using centrifugation (6.71 g).

Equipment and Analytical Methods. The synthesized nanomaterials were characterized through several methods: Dynamic Light scattering (DLS), Zeta Potential (ZP), scanning electron microscopy (SEM) and energy dispersive X-ray fluorescence (EDX), X-ray powder diffraction (XRD), confocal Raman and SERS spectroscopy, UV-visible absorption and Fourier-

transform infrared spectroscopy. The size distribution and ξ-potential of colloids were measured by DLS from Malvern Instruments Ltd. by using a Zetasizer Nano instrument and a prepared buffer solution.[35] DLS and ξ-potential (electrical charge) experiments were carried out on a 50 times diluted colloidal suspension. Each measurement took 10 s; the nanoparticle distribution and electrophoretic curves were obtained by averaging ten measurements. The morphology and elemental composition of sonochemically prepared nanomaterials were analyzed and characterized by SEM (S-4800) Hitachi, Japan. The phase composition was determined by using powder diffraction patterns recorded with an EMPYREAN diffractometer (PANalytical, Netherlands) using Cu-Kα radiation (Ni-filter) at 296 K.

Raman and SERS spectra were recorded by using a 3D scanning laser confocal Raman microscope Confotec NR500 (SOL Instruments Ltd., Republic of Belarus) at 633 nm excitation wavelength with a grating 600gr/mm blazed at 600 nm. The Si wafer with the characteristic Raman line at 520 cm^{-1} was taken as a reference for calibration and basic alignment during integration time from 1 to 3 s. The SERS-measurements were performed with the silvered porous silicon (Ag/PS) substrates described elsewhere[36] in order to enhance Raman signals of molecular compounds. The SERS-active substrates were kept in each freshly prepared aqueous colloidal solution for 2 hours and then taken out of glass vessels. Immediately afterwards incubated SERS-active substrates were rinsed with DI water and air-dried. The acquired Raman and SERS spectra were corrected for the baseline and a background of the SERS-active substrates based on Ag/PS. A linearly polarized diode laser beam was focused through the objectives with 40x and 100x magnification for Raman and SERS spectra acquisition. The laser power (4 mW) was attenuated by using neutral density filters with the following optical density (OD) values 0.6 (25), 0.3 (50) and no filter (100).

The crystallite size of carbonaceous nanostructures L_a (nm) was calculated by using the following equation[37] (1)

$$L_a = \frac{\left(2.4 \cdot 10^{-10}\right)\lambda_{laser}^{\ 4}}{Int_D / Int_G}, \qquad (1)$$

where L_a – the crystallite size of carbonaceous nanostructures (nm), λ_{laser} – the excitation laser wavelength (nm), Int_D/Int_G – the intensity ratio of Raman D and G lines.

The UV-visible absorption spectra of colloidal solutions were recorded by using a Cary-500 spectrophotometer (Varian, USA) in the wavelength range from 200 to 800 nm. The molecular structure of nanocomposites was revealed by FTIR Vertex 70 Bruker spectrometer (Germany) in the range from 400 to 4000 cm^{-1} by using Zeiss Jena Specord-75IR (Germany).

3. Results and Discussion

The main idea of the present work is illustrated in **Scheme 1**.

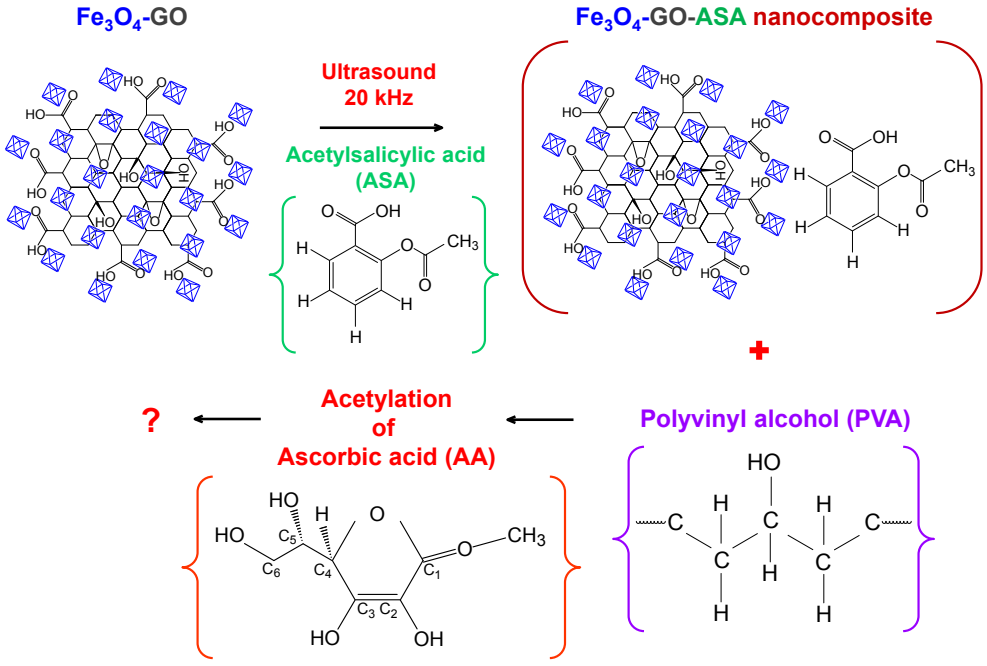

Scheme 1. Synthesized graphene oxide-Fe_3O_4 nanoparticles are used for the ultrasonic functionalization of pristine ASA (20 kHz, 18 W/cm^2) resulting in the formation of graphene oxide-Fe_3O_4-ASA nanocomposite as a final product. This product was ultrasonically coated with PVA in order to perform acetylation of pristine AA in aqueous solution.

In this work two goals are pursued: 1) sonochemical functionalization of pristine ASA with preformed graphene oxide-Fe_3O_4 nanoparticles (Fe_3O_4-GO) and 2) study of acetylation of pristine AA (AA) with graphene oxide-Fe_3O_4-ASA nanocomposites (Fe_3O_4-GO-ASA) coated with PVA and revealing the role of PVA in this reaction.

3.1 Morphology and composition of Fe_3O_4-GO nanoparticles

The sonochemically formed graphene oxide-Fe_3O_4 nanoparticles can be collected by the external permanent magnet in aqueous solution showing the magnetic nature of this material (**Figure 1A**). These nanoparticles have irregular cubic morphology with the mean size of 78 ± 9 nm (**Figure 1B** and **C**). **Figure 1D** shows SERS spectra of synthesized graphene oxide-Fe_3O_4 nanoparticles (red line) in comparison with pristine graphene oxide (black line). SERS spectrum of GO shows two peaks that can be assigned to K-point phonons of A_{1g} D breathing mode (~ 1340 cm^{-1}) and zone center phonons of E_{2g} G mode (~ 1603 cm^{-1}) with their intensity ratio Int_D/Int_G ~ 1.17, indicating that synthesized GO consists of mixture of amorphous and crystalline regions containing carbon with sp^2 hybridization.[38] The intensity of disorder-induced D mode is relatively low (~ 0.42) pointing out to a structural perfection of a carbon material.[39] The Full Width at Half Maximum (FWHM) of G mode (~ 57 cm^{-1}) is smaller than of D mode (~ 90 cm^{-1}), demonstrating relatively low structural disorder of GO that contains localized sp^2 dimers or shorter sp^2 chains with a sharper length distribution.[40] The crystallite size of GO is ~ 32.92 nm according to eq. (1). The surface structure of GO was examined by FTIR absorption

spectroscopy (Figure S1, Supporting Information). FTIR spectrum of GO shows strong vibrational bands of C-O at ~ 1103 cm^{-1}, $_{\nu}$(COO) in COO^- at ~ 1459 cm^{-1}, aromatic and unsaturated bands $_{\nu}$(COO) in ($HCOO^-$) of carboxylic group at ~1570 cm^{-1}, C=C at ~ 1628 cm^{-1}, -C=O of carboxylic group at ~1743 cm^{-1}, asymmetric and symmetric C-H stretching vibrations at ~2854 cm^{-1} and ~2927 cm^{-1}, and O-H stretching band at ~3433 cm^{-1},[41] demonstrating that oxidation process during the synthesis of GO resulted in the formation of hydroxyl and carboxylic groups with the presence of aromatic regions, typical for oxidized graphene nanoribbons.[42] However, the surface of synthesized GO doesn't contain epoxide groups because the characteristic C-O bands at 1220-1225 cm^{-1} are absent. The presence of carboxyl and hydroxyl groups on the surface of synthesized GO with aromatic regions points out that GO retains its functionality with enhanced electronic properties, which can be used for more efficient acetylation of ascorbic acid.

In contrast, SERS spectrum of Fe_3O_4-GO nanoparticles shows multiple peaks that can be assigned to Fe(II)-CO (~ 480 and 525 cm^{-1}),[41] Fe_3O_4 (~ 554, 626 and 660 cm^{-1}),[43] γ-Fe_2O_3 (~ 725 and 765 cm^{-1}),[44] epoxide group of GO (~ 853 cm^{-1}),[45] Fe-O (~ 1038 cm^{-1}),[46] $FeCO_3$ (~ 1080 cm^{-1})[47] (**Figure 1D**, red line). Vibrational bands at ~ 1160 and 1425-1465 cm^{-1} can be assigned to GO that correspond to nanocrystalline diamond as a result of the sum and difference modes of C-C with sp^2 hybridization and C–H vibrations of transpolyacetylene type segments occurring at grain boundaries.[48] The presence of H-ending C=C chain was observed at ~ 1160 cm^{-1} and aromatic carbonate at ~ 1221 cm^{-1}.[49]

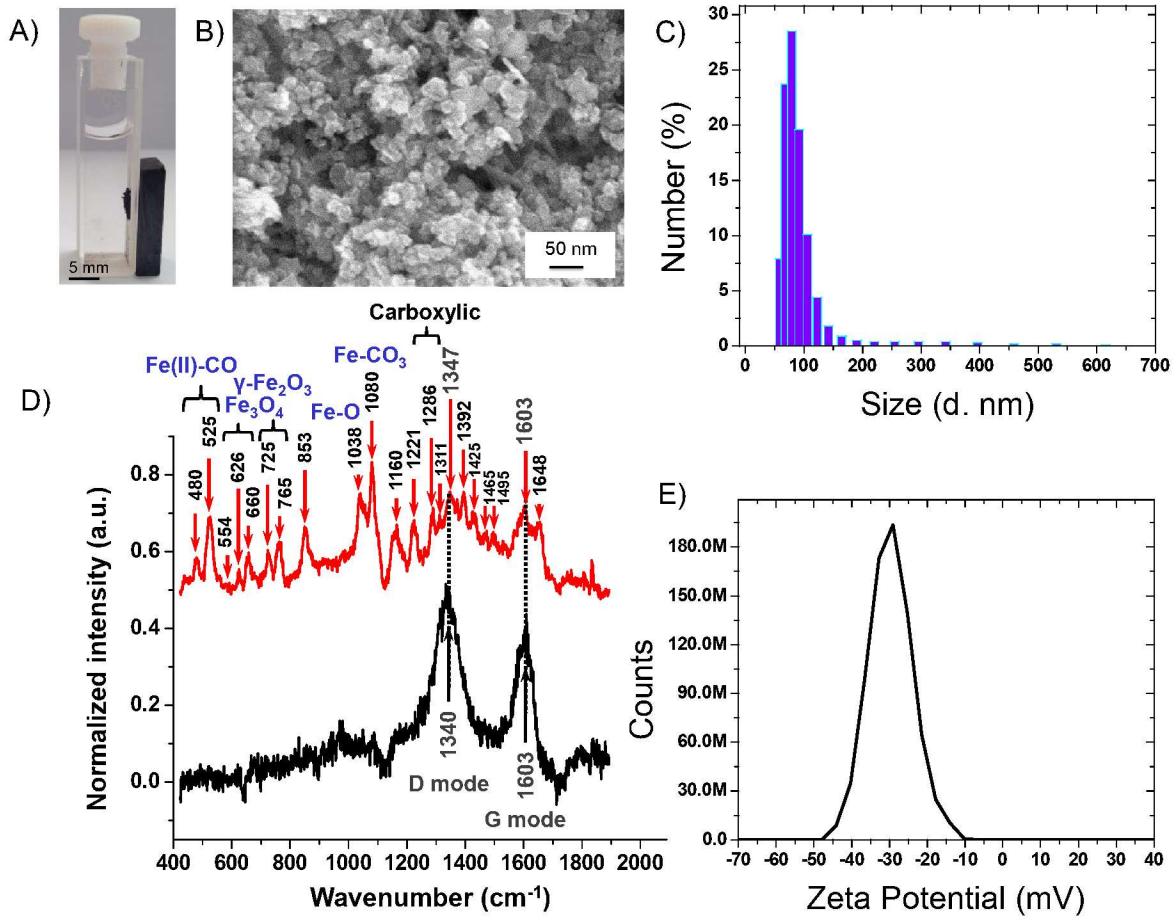

Figure 1. A) True color photo image of sonochemically synthesized graphene oxide-Fe_3O_4 nanoparticles that can be collected by an external permanent magnet. B) Representative SEM image and C) DLS size distribution diagram showing morphology of these nanoparticles of < 100 nm. D) SERS spectra of synthesized graphene oxide (black line) and sonochemically formed graphene oxide-Fe_3O_4 nanoparticles (red line). E) Zeta potential plot of prepared graphene oxide-Fe_3O_4 nanoparticles demonstrating the negative surface charge.

Carboxylic acid groups can be revealed by their characteristic Raman peaks at 1286 and 1311 cm^{-2} in the nanocomposite. The D mode is shifted at ~ 1347 cm^{-1} and the G mode (~ 1603 cm^{-1}) developed a shoulder at 1648 cm^{-1}, demonstrating the changes of the dimensions

and structural ordering of the layers that can be caused by the formation of Fe_3O_4-GO nanocomposite.[50] The intensity ratio Int_D/Int_G is ~ 0.82, demonstrating the lower total number of defects that are present in nanocomposite than in GO. The calculated FWHM values of D and G lines are smaller in Fe_3O_4-GO than in GO and the G peak (~ 33 cm^{-1}) is broader than the D peak (~ 20 cm^{-1}), pointing out that the formation of nanocomposite did not destroy the chemical bonds of graphene and didn't break its structure. The crystallite size of Fe_3O_4-GO nanocomposite is ~ 47.27 nm, which is larger than that of GO. This small peak at 1648 cm^{-1} can arise from non-regular rings in a C divacancy.[51]

The Zeta potential of Fe_3O_4-GO nanocomposites is -29.9 ± 6.3 mV (**Figure 1E**) due to the presence of O (49.6 ± 4.1 at.%), C (26.9 ± 1.9 at.%) and Fe (20.4 ± 1.4 at.%) as revealed from the EDS analysis (**Figure S2** and **Table S1**).

3.2 Crystalline and electronic molecular structure of Fe_3O_4-GO nanoparticles

The phase composition and crystalline structure of Fe_3O_4-GO nanocomposites were revealed from X-Ray powder diffraction patterns (**Figure 2A**) and the experimental data were compared with synthesized GO (**Table 1** and **2**). The XRD diagram of graphene oxide shows an elevated continuum with several small peaks at 2θ = 12.24 and 38.36 arising from GO,[52] 34.95 and 40.12 indicating the presence of diamond phase and 42.71 due to graphite phase that is in agreement with the crystallographic database of diamond (amcsd 0013983) and graphite (amcsd 0000049) (Figure 2A and Table 1).

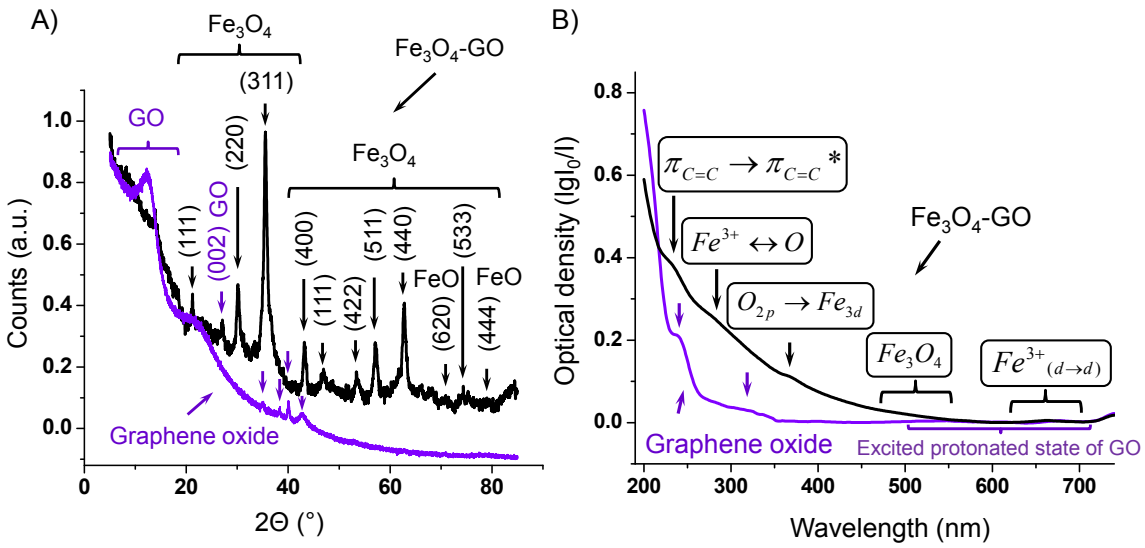

Figure 2. A) X-Ray powder diffraction patterns and B) UV-visible absorption spectra of synthesized graphene oxide (GO) and sonochemically formed Fe_3O_4-GO nanoparticles.

A broad small peak of at $2\theta = 12.24$ points out to the heterogeneous structure of GO containing graphite domains with sp^2 and sp^3 hybridization.[53]

Table 1. X-Ray powder diffraction data of synthesized graphene oxide (GO).

2θ, °	**I, a.u.**	**(hkl)**	**d_{hkl}, Å**	**Material (Phase)**
12.24	8	(001)	7.07	GO
34.95	1	(020)	2.56	GO (diamond)
38.36	1	-	2.35	GO
40.12	2	(021)	2.27	GO (diamond)
42.71	1	(020)	2.12	GO (graphite)

The XRD pattern of sonochemically synthesized Fe_3O_4-GO nanoparticles shows characteristic reflexes of Fe_3O_4 crystalline phase (amcsd 0020645) with changed *d* interplanar spacing values due to the effect of pressure gradient (Table 2). The calculated *d* values point out

to the effect of pressure gradient from ~ 1 atm (≈ 10^{-4} GPa) to ~ 1-20·10^3 atm (< 2 GPa) that can be produced in cavitation hot spots.[54] The XRD diagram reveals the presence of FeO (amcsd 0013895) and a possible recoverable high-pressure and high-temperature polymorph of iron oxide Fe_4O_5 (amcsd 0018509).[55] Fe_4O_5 can be produced upon heating at 1500-2200 K as a result of a breakdown of magnetite into one of iron oxide phases depending on the pressure gradient. The recently discovered phase Fe_4O_5 can result from the breakdown of magnetite into Fe_4O_5 and Fe_2O_3. However, the XRD pattern of Fe_3O_4-GO nanoparticles shows only reflexes of Fe_3O_4 and FeO phases. Therefore the presence of high pressure Fe_4O_5 phase is less probable.

Table 2. X-Ray powder diffraction data of sonochemically formed Fe_3O_4-GO nanoparticles.

2θ, °	**I, a.u.**	**(hkl)**	**d_{hkl}, Å**	**Material (Phase)**
8.08	9	-	11.61	GO
13.92	19	-	6.53	GO
18.38	11	(111)	4.82	Fe_3O_4
21.26	15	(001)	4.10	GO (diamond)
27.07	13	(002)	3.33	GO (graphite)
30.18	30	(220)	2.96	Fe_3O_4
35.51	100	(311)	2.53	Fe_3O_4
43.20	23	(400)	2.09	Fe_3O_4
46.96	11	(111)	1.92	GO (graphite)
48.46	7	(112)	1.85	GO (diamond)
51.53	5	(220)	1.78	GO (diamond)
53.36	13	(422)	1.72	Fe_3O_4
57.13	26	(511)	1.61	Fe_3O_4
62.73	41	(440)	1.48	Fe_3O_4

66.19	8	(222)	1.40	GO (diamond)
68.27	9	(132)	1.36	GO (diamond)
70.90	7	(620)	1.33	FeO
74.44	11	(533)	1.27	Fe_3O_4
78.73	6	(444)	1.21	FeO

As next, we examined the electronic molecular structure of Fe_3O_4-GO nanoparticles by using UV-visible absorption spectroscopy (**Figure 2B**). The absorption spectrum of GO exhibits two bands: at ~ 236 nm (5.28 eV) arising from the π–π* transition of aromatic C=C bonds and ~320 nm (3.88 eV) as a result of the n–π* transition of C=O bonds. In contrast, the UV-visible absorption spectrum of Fe_3O_4-GO nanoparticles is manifold with bands on elevated continuum that can be assigned to the $\pi_{c=c} \rightarrow \pi_{c=c}^*$ transition in GO comparable to graphene quantum dots;[56] $Fe^{3+} \leftrightarrow O$ (4.31 eV), $^6A1 \rightarrow {}^4T1(4p)$ (4.12 eV) and $O_{2p} \rightarrow Fe_{3d}$ (3.41 eV, isosbestic point of Fe_3O_4 nanoparticles) as a result of the enhanced electronic conjugation of graphene,[57] the intervalence charge transfer between Fe^{3+} and O existing in magnetite nanocrystals and Fe-O bonds in the carbonaceous network of GO[58] and $Fe^{3+}(d \rightarrow d)$ (1.79 eV) in conjunction with the excited protonated state of GO.

3.3 Ultrasonic complexation of ASA with Fe_3O_4-GO nanoparticles

Synthesized Fe_3O_4-GO nanoparticles were used for ultrasonic complexation with pristine ASA resulting in formation of ASA-Fe_3O_4-GO nanoparticles. The UV-visible absorption spectroscopy was used to find out how ASA is complexed with Fe_3O_4-GO nanoparticles and what is the role of GO and magnetite in this process (**Figure 3**).

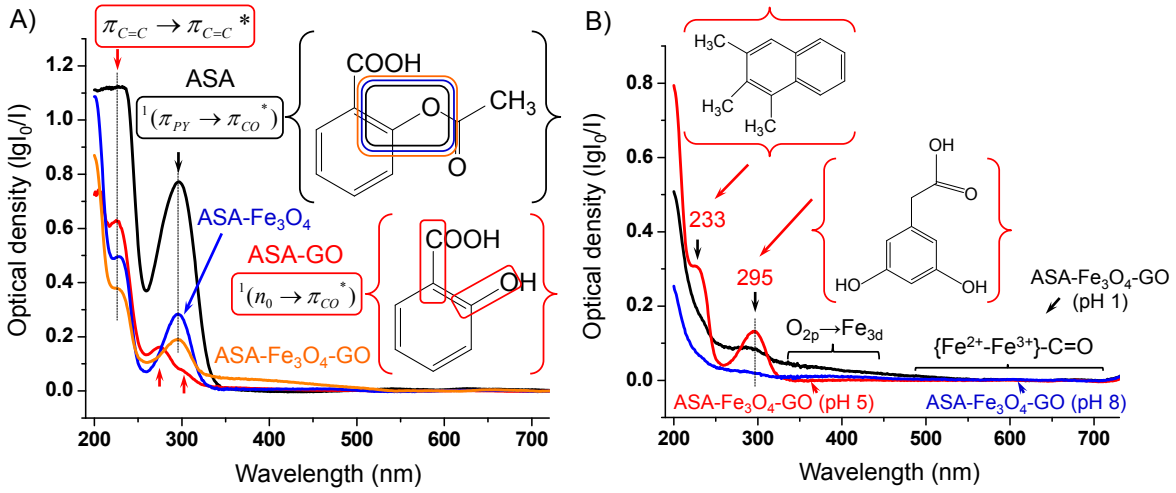

Figure 3. UV-visible absorption spectra of A) pristine ASA (black line), ASA-Fe_3O_4-GO nanoparticles (orange line) in comparison with ASA-GO (red line) and ASA-Fe_3O_4 (blue line) after sonication (20 kHz, 18 W/cm^2) in aqueous solution and B) ASA-Fe_3O_4-GO nanoparticles after aging in DI water at pH 1, 5 or 8.

UV-visible absorption spectrum of ASA-Fe_3O_4-GO nanoparticles in aqueous solution exhibits two bands: at 226 nm (~ 5.49 eV) due to the $\pi_{c=c} \rightarrow \pi_{c=c}^*$ transition in GO and 295 nm (~ 4.20 eV) arising from the $^1(\pi_{py} \rightarrow \pi_{co}^*)$ transition of the π (bonding) molecular orbital from the phenyl ring in –C=C- or C=O to its π* (anti-bonding) orbital in the ASA[59] and $^1(n_0 \rightarrow \pi_{co}^*)$ transition in C=C or C=O of the carboxylic groups in salicylic acid[60] (**Figure 3A**). For comparison, aqueous solution of pristine ASA exhibits strong absorption band in the region from ~ 200-250 nm and characteristic peak at ~ 296 nm that is indicative of ASA functional groups.[61] The first broad band overlaps with the characteristic absorbance of pristine GO (~ 236 nm). ASA-Fe_3O_4 nanoparticles in aqueous solution exhibit absorption bands similar to ASA-Fe_3O_4-GO with GO peak being red shifted at ~ 228 nm (~ 5.44 eV) that can be caused by the changes of the methyl group in ASA. In contrast, UV-visible absorption spectrum of ASA-GO

nanoparticles shows two bands: at 277 nm (ASA) and 302 nm (salicylic acid). The OD values of ASA band in all types of nanoparticles vary from highest to lowest in the following order: pristine ASA → ASA-Fe_3O_4 → ASA-Fe_3O_4-GO → ASA-GO (**Table 3**). The ratio OD (pristine ASA)/OD (type of ASA nanoparticle) is the highest in ASA-GO and the lowest in ASA-Fe_3O_4, pointing out to the difference in the binding affinity of ASA to GO and magnetite components and their catalytic activity in the Fe_3O_4-GO structure. Magnetite may enhance the electronic density of ASA in ASA-Fe_3O_4-GO nanocomposite and GO may control the electron charge transfer of ASA and accelerate the acetylation.

Table 3. UV-visible absorption data of pristine ASA, ASA-Fe_3O_4, ASA-GO and ASA-Fe_3O_4-GO nanoparticles in aqueous solution.

Compound	Peak, nm	Optical density (lgI_0/I), a.u.	Ratio*, a.u.
pristine ASA	296	0.77	1
ASA-GO	277 and 302	0.17 and 0.08	4.53 and 9.63
ASA-Fe_3O_4	295	0.29	2.66
ASA-Fe_3O_4-GO	295	0.20	3.91
pristine GO	236	1.12	1
ASA-GO	227	0.64	1.75
ASA-Fe_3O_4	228	0.50	2.25
ASA-Fe_3O_4-GO	226	0.38	2.95

*Ratio is calculated by dividing the optical density (OD) value of pristine ASA or GO (in italic) with the OD magnitudes of ASA-GO, ASA-Fe_3O_4 and ASA-Fe_3O_4-GO.

The stability of ultrasonically formed ASA-Fe_3O_4-GO nanoparticles was examined by aging aqueous colloidal solutions adjusted at pH 1, 5 or 8 and recording UV-visible absorption spectra (**Figure 3B**). After the treatment the most intense absorbance of ASA-Fe_3O_4-GO nanoparticles was observed at pH 5 with the appearance of bands at ~233 nm (characteristic of ASA with

naphthalene-trimethyl structure) and 295 nm. These bands became smoothed on elevated absorption continuum at pH 1 and almost vanished at pH 8. At pH 1 the broadening of the characteristic ASA peak at 295 nm was accompanied with an absorbance near 400 nm and 600 nm, demonstrating the presence of dihydroxyphenyl acetic acid structure of the salicylic acid because of its complexation with ferrous ions that can be formed as reaction products of Fe_3O_4 dissolution in acidified water.[61] Heating during acoustic cavitation may favor the solubilization of salicylic acid in water with intramolecular H-bonding capable of protolytic dissociation, i.e. exchange in the intramolecular proton movements in the salicylic acid and its specific binding to Fe_3O_4-GO because of the excited multiple $O_{2p}\rightarrow Fe_{3d}$ and $\{Fe^{2+}\text{-}Fe^{3+}\}$@C=O transitions. The contribution of $O_{2p}\rightarrow Fe_{3d}$ transitions and H-bonding in ASA-Fe_3O_4-GO structure is negligible at pH 5, but not at pH 8 because absorbed water molecules have a specific effect on the stability of the ASA-Fe_3O_4 complex in a basic aqueous medium. Quantum chemical calculations reveal that the dimer with two H-bonds can be more stable through two carboxyl groups via the charge transfer and electrostatic interaction,[63] in agreement with the absorption bands in the 200-300 nm spectral range. This is because the *n* electrons of anions of organic acids in the GO structure are highly affected by the H-bond formation. The energy levels of *n* electrons decrease significantly in water and this causes a shift in an absorption maximum of an $n\rightarrow\pi^*$ transition, which is almost equal to the energy of the formed H-bond. The decreased intensity of the peak at 295 nm indicates the expanded polarity of water as a consequence of the increased solvation of *n* electrons.

3.4 Effect of PVA on acetylation of ascorbic acid by ASA-Fe_3O_4-GO nanocomposites

As next, the ability of sonochemically formed ASA-Fe_3O_4-GO nanoparticles to acetylate AA was examined by SERS spectroscopy in comparison with ASA-Fe_3O_4-GO-PVA and pristine AA

being thermally treated with ASA in order to reveal the role of PVA in this reaction (**Figure 4**). The detailed assignment of vibrational bands of thermally treated pristine AA, AA acetylated by ASA-Fe_3O_4-GO and ASA-Fe_3O_4-GO-PVA nanoparticles can be found in the Supporting Information (**Table S2**). SERS spectra are shown in the region 250-1000 cm^{-1} (**Figure 4A**) and 900-2000 cm^{-1} (**Figure 4B**). SERS spectra of AA acetylated with ASA-Fe_3O_4-GO or ASA-Fe_3O_4-GO-PVA nanoparticles didn't reveal any bands in the region 2000-3500 cm^{-1}, therefore they are not shown. For comparison, we also performed Raman and SERS measurements and spectral analysis of free pristine AA (**Figure S3** and **Table S3**), ASA (**Figure S4** and **Table S4**) and PVA (**Figure S5** and **Table S5**). Control experiments were performed by thermal treating of ASA-Fe_3O_4-GO and ASA-Fe_3O_4-GO-PVA without AA (more details about spectral analysis can be found in the Supporting Information, **Figure S6** and **S7**, **Table S6** and **S7**), and of pristine AA without nanoparticles (**Figure S8** and **Table S8**).

The SERS spectrum of pristine AA thermally treated with ASA shows most of characteristic bands of AA[64] (Figure S3 and Table S3) with several shifted peaks at ~ 448 cm^{-1} (OH wagging of AA*a and $\delta_A(OCOCH_3)$ + $\gamma_A(CC)_{rings}$ of ASA),[65] ~ 1042 cm^{-1} (C_1–O_4, C_3–C_4, C_6–O_6 stretching of AA and $\delta_s(CH)_{rings}$ of ASA), ~ 1195 cm^{-1} (C-O-H bending of AA and ν_{as}(O-CO-CH_3) + $\delta_{as}(CH_3)$ of ASA) and ~ 1367 cm^{-1} (C_1-C_2, C_3-C_4 stretching and ring OH bending of AA and $\delta_{ss}(CH_3)$ of ASA), demonstrating acetylation of ascorbic by ASA. Two Raman bands of AA that appear without shift at 423 cm^{-1} and 1607 cm^{-1} can be assigned to {C_6-O_6 torsion of AA and $\delta_A(O\text{-}CO\text{-}CH_3)_{sciss}$ + $\gamma_A(CC)_{rings}$ of ASA} and { C_1-O_1, C_2-C_3, C_2-O_2 stretching of AA and $\nu_s(CC)_{rings}$ of ASA} due to binding of AA with ASA.

SERS spectrum of ASA-Fe_3O_4-GO-ascorbic acid nanoparticles shows characteristic bands of ascorbic acid (Figure S3 and Table S3), magnetite at ~ 671 cm^{-1} with γ-Fe_2O_3 phase (~ 763 cm^{-}

[1]), Fe-C-O (~ 1080 cm^{-1}) and Fe-C (~ 1338 cm^{-1}) along with A_{1g} D mode and E_{2g} G mode of graphene oxide (~ 1582 cm^{-1}) of graphene oxide, indicating the strong binding of AA with magnetite within carbonaceous network of graphene (Figure 4 and Table S2). Raman bands: at ~ 1190 cm^{-1} that is assigned to {C-C(-O)-O stretching AA and ν_{as}(O-CO-CH_3) + δ_{as} (CH_3) of ASA}, ~ 1363 cm^{-1} to { C_1-C_2, C_3-C_4 stretching and ring OH bend. of AA, δ_{sS}(CH_3) of ASA} and ~ 1461 cm^{-1} to { C-H bending of AA and δ_s(OH) + δ_{as}(CH_3) + δ_s($CH)_{rings}$ of ASA} demonstrate the binding of methyl groups of ASA to AA.

SERS spectrum of ASA-Fe_3O_4-GO-PVA-ascorbic acid nanoparticles reveals several bands of pristine AA and AA along with characteristic peaks of Fe(II)-CO and CO of PVA (~ 488 cm^{-1}), CO of AA with Fe(II)-CO (~ 572 cm^{-1}), magnetite (~ 676 cm^{-1}) with γ-Fe_2O_3 phase and ring deformation of AA (~ 729 cm^{-1} and ~ 766 cm^{-1}) and C_4 bending of AA with γ(CH_2) of PVA (~ 823 cm^{-1}), demonstrating that binding of PVA with AA occurs involving Fe-C-O and magnetite. Raman A_{1g} D mode of GO is shifted at ~ 1327 cm^{-1} with Fe-C and a peak of E_{2g} G mode remains (~ 1581 cm^{-1}) in the polymer matrix due to the appearance of several PVA vibrational bands. In contrast to ASA-Fe_3O_4-GO-ascorbic acid nanoparticles (without PVA), this nanocomposite exhibits more Raman bands: at ~ 423 cm^{-1} that is assigned to {C_6-O_6 torsion of AA and δ_s(O-CO-CH_3) + γ_s(C-C) of ASA}, ~ 448 cm^{-1} to {OH wagging of AA* and δ_s(O-CO-CH_3) + γ_s(C-C) of ASA}, ~ 901-943 cm^{-1} to {δ_s(CC) rings + δ_s(O-CO-CH_3) of ASA}, ~ 1008-1013 cm^{-1} to {(O-CO-CH_3) + CH_3 of ASA}, ~ 1191-1208 cm^{-1} to {(C-H) AA, ν_{as}(O-CO-CH_3) + δ_{as} (CH_3) ASA, ν_s(CC + CO) PVA}, ~ 1220 cm^{-1} to {ν_s(Ph-O-CO-CH_3) + δ_s($CH)_{rings}$ of ASA} and ~ 1370 cm^{-1} to {C_1-C_2, C_3-C_4 stretching and ring OH bend. of AA, δ_{sS}(CH_3) of ASA}, pointing out to the more effective acetylation of AA by ASA in the presence of PVA and magnetite bonded to GO.

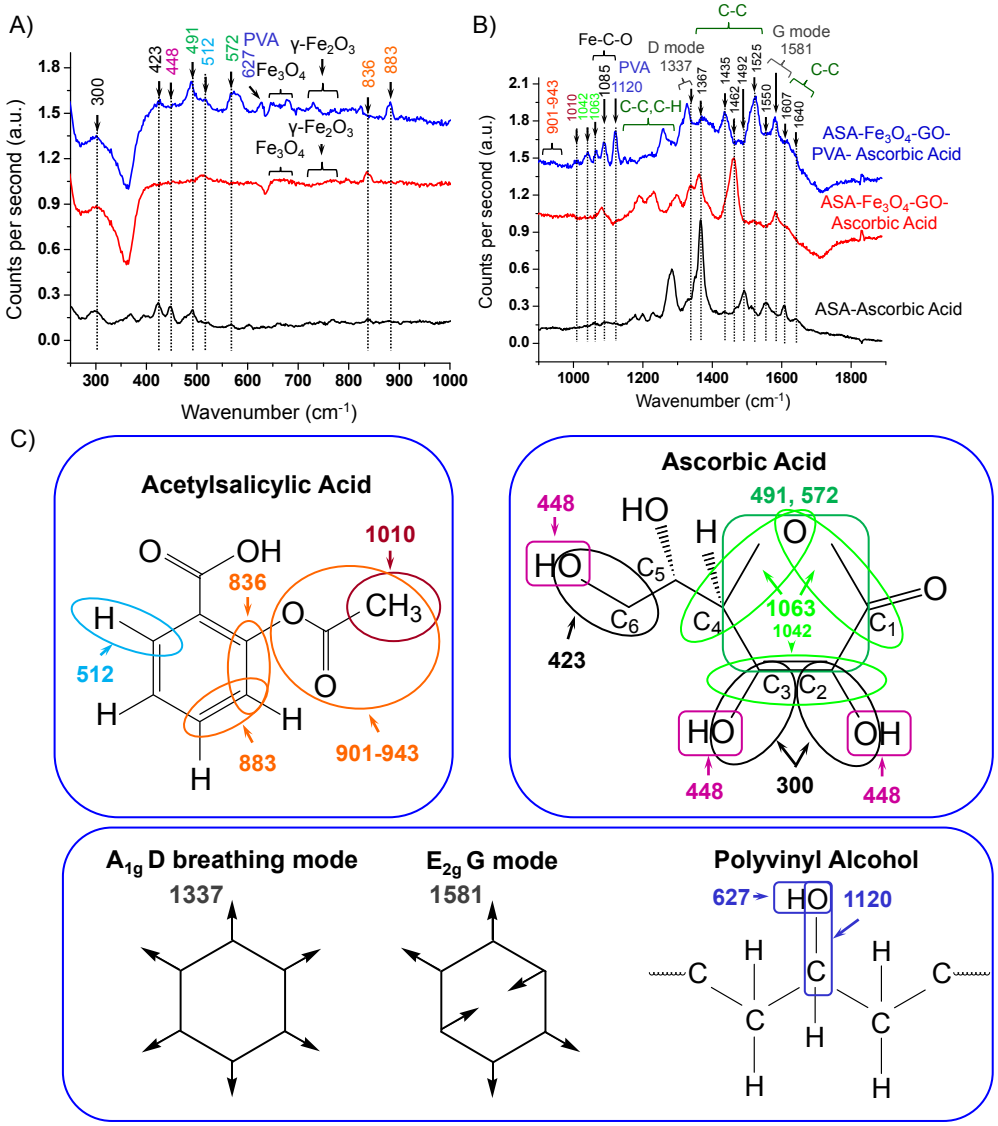

Figure 4. A) and B) SERS spectra of pristine ascorbic acid after thermal treating with ASA at T ≈ 80°C (black line) and ascorbic acid acetylated by ASA-Fe_3O_4-GO (red line) and ASA-Fe_3O_4-GO-PVA (blue line) nanocomposites (λ_{exc} = 633 nm) after thermal stirring at T ≈ 80 °C for 60 min. C) Schematic illustration of chemical structures of ASA, ascorbic acid and PVA with defined Raman chemical vibrational bonds obtained from spectra.

In addition, several distinct Raman bands at ~ 627 cm^{-1} (C_4-C_5 stretching and ring deformation of AA and γ(OH) of PVA[66]), ~ 823 cm^{-1} (C_4 on plane bending of AA and γ(CH_2)

of PVA) that are assigned to AA with PVA; and ~ 646 cm^{-1} ($\delta_s(CC)_{rings}$ + δ_s(O-C=O) + δ_s(COOH) of ASA and $\gamma(OH)_{twist}$ of PVA), ~ 1147 cm^{-1} ($\delta_s(CH)_{rings}$ of ASA and ν_s(CC + CO) of PVA) and ~ 1435 cm^{-1} ($\delta_{aS}(CH_3)$ of ASA, $\delta(CH_2)$ of PVA) that are assigned to ASA with PVA demonstrate that PVA enhances specific interaction with AA and also ASA.

4. Conclusions

A new ultrasonic single step method (20 kHz) was demonstrated for the formation of ASA-Fe_3O_4-graphene oxide nanocomposites (78 ± 9 nm) in aqueous solution. These superparamagnetic nanoparticles have a stable electronic molecular structure with increased electron density due to the specific binding of magnetite with GO. ASA-Fe_3O_4-GO nanocomposites exhibit more efficient acetylation of AA in comparison with free pristine ASA. Coating of these nanocomposites with PVA significantly enhances acetylation of pristine AA (AA) due to the stronger binding of polymer to ASA, AA, magnetite and GO involving Fe(II)-C-O. This new knowledge substantially refines our understanding about the improvement of pharmaceutical function of ASA and discloses the important role of biocompatible polymer, iron oxide and graphene oxide nanoparticles in it.

Supporting Information.

The following files are available free of charge.

Synthesis of GO; FTIR absorption spectrum of GO; Energy Dispersive X-Ray fluorescence spectra of synthesized Fe_3O_4-GO nanoparticles; SERS spectra and analysis of pristine ascorbic acid with ASA, ascorbic acid with ASA-Fe_3O_4-GO or ASA-Fe_3O_4-GO-PVA nanocomposites after thermal stirring at T ≈ 80°C for 60 min; Raman and SERS spectra and analysis of aqueous solutions of free unmodified ascorbic acid, ASA and PVA; Raman spectra of thermally treated (T ≈ 80°C for 60 min) ASA-Fe_3O_4-GO and ASA-Fe_3O_4-GO-PVA nanoparticles (without ascorbic acid).

Corresponding Author

*Darya Radziuk, E-mail: radziuk@bsuir.by

Author Contributions

The manuscript was written through contributions of all authors. All authors have given approval to the final version of the manuscript.

Funding Sources

This work is supported by the BRFFR grant № 16-3041 57 031.00 and MOST Belarus-EU financial program through grants № R-YPQZ-53145 and 57111R-dDMu-57100.

Acknowledgment

Prof. Mikhail Artemyev and Prof. Ludmila Ivashkevich from the Belarusian State University (Minsk) are gratefully acknowledged for the ZP/DLS, XRD measurements and constructive discussions.

References

1. Patrono, C.; Baigent,C. Role of aspirin in primary prevention of cardiovascular disease. *Nat. Rev. Cardiol.*, **2019**, *16*, 675-686.
2. Chen, W. Y.; Holmes, M. D. Role of aspirin in breast cancer survival. *Curr. Oncol. Rep*., **2017**, *19*, 1-48.
3. Patrignani, P.; Patrono, C. Aspirin and cancer. *JACC*, 2016, 68, 967-976.
4. Alfonso, L.; Ai, G.; Spitale, R. C.; Bhat, G. J. Molecular targets of aspirin and cancer prevention. *Brit. J Cancer*, **2014**, *111*, 1-7.
5. Jane, V. Towards a better aspirin. *Nature*, **1994**, *367*, 215-216.
6. Rouzer, C. A.; Marnett, L. J. Cyclooxygenases: structural and functional insights. *J Lipid Res*., **2009**, *50*, S29-S34.
7. Banti, C. N.; Hadjikakou, S. K. *Eur. J. Inorg. Chem.,* **2016**, *2016*, 3048-3071.
8. Metal ions on biological systems. Ed. A. Sigel and H. Sigel, Volume 41: Metal ions and their complexes in medication. 2004, CRC Press, 600 p.
9. Leung, C.-H.; Lin, S.; Zhong, H.-J.; Ma, D.-L. Metal complexes as potential modulators of inflammatory and autoimmune responses. *Chem. Sci.*, **2015**, *6*, 871-884.
10. Sun, Y.; Heidary, D. K.; Zhang, Z.; Richards, C. I.; Glazer, E. C. Bacterial cytological profiling reveals the mechanism of action of anticancer metal complexes. *Mol. Pharmaceutics*, **2018**, *15*, 3404-3416.
11. Banti, C. N.; Papatriantafyllopoulou, C.; Tasiopoulos, A. J.; Hadjikakou, S. K. New metalo-therapeutics of NSAIDs against human breast cancer cells. *Eur. J Med Chem.*, **2018**, *143*, 1687-1701.
12. Vitorino, H. A.; Mantovanelli, L.; Zanotto, F. P.; Espósito, B. P. Iron metallodrugs: stability, redox activity and toxicity against artemia salina. *PLoS ONE* **2015**, *10*, e0121997.
13. Crichton R., Iron metabolism: from molecular mechanisms to clinical consequences, 4th Ed., Chapter 2: The essential role of iron in biology. John Wiley & Sons, Ltd., 2016, p. 556.
14. Abbaspour, N.; Hurrell, R.; Kelishadi, R. Review on iron and its importance for human health. *J Res. Med. Sci.*, **2014**, *19*, 164-174.
15. Iqbal, M. S.; Khurshid, S. J.; Muhammad, B. Anti-inflammatory and selective COX-2 inhibitory activities of metal complexes of Schiff bases derived from aldoses. *Med. Chem. Res.,* **2013**, *22*, 861-868.
16. Wu, Y.; Li, L.; Frank, L.; Wagner, J.; Andreozzi, P.; Hammer, B.; D'Alicarnasso, M.; Pelliccia, M.; Liu, W.; Chakrabortty, S.; Krol, S.; Simon, J.; Landfester, K.; Kuan, S. L.; Stellacci, F.; Müllen, K.; Kreppel, F.; Weil, T. Patchy amphiphilic dendrimers bind

adenovirus and control its host interactions and in vivo distribution. *ACS Nano* **2019**, *13*, 8749-8759.

17. Litti, L.; Reguera, J.; García de Abajo, F. J.; Meneghetti, M.; Liz-Marzán, L. M. Manipulating chemistry through nanoparticle morphology. *Nanoscale Horiz.*, **2020**, *5*, 102-108.
18. Massart, R. Preparation of aqueous magnetic liquids in alkaline and acidic media. *IEEE transactions on magnetics*, **1981**, *17*, 1247-1248.
19. Daou, T. J.; Pourroy, G.; Bégin-Colin, S.; Grenèche, J. M.; Ulhaq-Bouillet, C.; Legaré , P.; Bernhardt, P.; Leuvrey, C.; Rogez, G. Hydrothermal synthesis of monodisperse magnetite nanoparticles. *Chem. Mater.*, **2006**, *18*, 4399-4404.
20. Vijayakumar, R.; Koltypin, Yu.; Felner, I.; Gedanken, A. Sonochemical synthesis and characterization of pure nanometer-sized Fe_3O_4 particles. *Mater. Sci. Eng.*, **2000**, *A286*, 101-105.
21. Radziuk, D.; Mikhnavets, L.; Vorokhta, M.; Matolín, V.; Tabulina, L.; Labunov, V. Sonochemical formation of copper/iron-modified graphene oxide nanocomposites for ketorolac delivery. *Chem. Eur. J.,* **2019**, *25*, 6233-6245.
22. Fiadosenka, U.; Matsukovich, A.; Tabulina, L.; Labunov, V.; Radziuk, D. The properties of the sonochemically functionalized nonsteroidal anti-inflammatory drug ketorolac in an Fe_3O_4–graphene oxide nanocomposite. *New J Chem.*, **2019**, *41*, 16118-16122.
23. Ma, D.; Chen, J.; Luo, Y.; Wang, H.; Shi, X. Zwitterion-coated ultrasmall iron oxide nanoparticles for enhanced T1-weighted magnetic resonance imaging applications. *J. Mater. Chem. B*, **2017**, *5*, 7267-7273.
24. Lal, M.; Verma, S. R. Synthesis and characterization of polyvinyl alcohol functionalized iron oxide nanoparticles. *Macromol. Symp*., **2017**, *376*, 1700017.
25. Deng, J.; He, C. L.; Peng, Y.; Wang, J.; Long, X.; Li, P.; Chan, A. S. C. Magnetic and conductive Fe_3O_4-PANI nanoparticles with core-shell structure. *Synth. Metals*, **2003**, *139*, 295-301.
26. Jain, T. K.; Morales, M. A.; Sahoo, S. K.; Leslie-Pelecky, D. L.; Labhasetwar, V. Iron oxide nanoparticles for sustained delivery of anticancer agents. *Mol. Pham*., **2005**, *2*, 194-205.
27. Rezvantalab, S.; Drude, N. I.; Moraveji, M. K.; Güvener, N.; Koons, E. K.; Shi, Y.; Lammers, T.; Kiessling, F. PLGA-based nanoparticles in cancer treatment. *Front. Pharmacol.*, **2018**, *9*, 1260-1-19.
28. Polymeric nanoparticles as a promising tool for anti-cancer therapeutics. Ed. Kesharwani, P.; Paknikar, K. M.; Gajbhiye, V.; Academic Press Elsevier, 2019, p. 432.
29. Fadeel, B.; Bussy, C.; Merino, S.; Vázquez, E.; Flahaut, E.; Mouchet, F.; Evariste, L.; Gauthier, L.; Koivisto, A. J.; Vogel, U.; Martin, C.; Delogu, L. G.; Bürki-Thurnherr, T.;

Wick, P.; Beloin-Saint-Pierre, D.; Hischier, R.; Pelin, M.; Carniel, F. C.; Tretiach, M.; Cesca, F.; Benfenati, F.; Scaini, D.; Ballerini, L.; Kostarelos, K.; Prato, M.; Bianco, A. Safety assessment of graphene-based materials: focus on human health and the environment. *ACS Nano*, **2018**, *12*, 10582-10620.

30. Martín, C.; Kostarelos, K.; Prato, M.; Bianco, A. Biocompatibility and biodegradability of 2D materials: graphene and beyond. *Chem. Commun*., **2019**, *55*, 5540-5546.
31. Pinto, A. M.; Moreira, J. A.; Magalhães, F. D.; Gonçalves, I. C.; Gonçalves, I. Polymer surface adsorption as a strategy to improve the biocompatibility of graphene nanoplatelets. *Colloid Surf. B*., **2016**, *146*, 818-824.
32. Marcano, D. C.; Kosynkin, D. V.; Berlin, J. M.; Sinitskii, A.; Sun, Z.; Slesarev, A.; Alemany, L. B.; Lu, W.; Tour, J. M. Improved synthesis of graphene oxide. *ACS Nano*, **2010**, *4*, 4806-4814.
33. Edwards, L. J. The dissolution and diffusion of aspirin in aqueous media. *Trans. Faraday Soc*., **1951**, *47*, 1191-1210.
34. Margulis, M. A.; Margulis, I. M. Calorimetric method for measurement of acoustic power absorbed in a volume of a liquid. *Ultrason. Sonochem*., **2003**, *10*, 343-345.
35. Radziuk, D.; Mikhnavets, L.; Tkach, A.; Tabulina, L.; Labunov, V. Sonochemically assembled photoluminescent copper-modified graphene oxide microspheres. *Langmuir*, **2018**, *34*, 8599-8610.
36. Zavatski, S.; Khinevich, N.; Girel, K.; Redko, S.; Kovalchuk, N.; Komissarov, I.; Lukashevich, V.; Semak, I.; Mamatkulov, K.; Vorobyeva, M.; Arzumanyan, G.; Bandarenka, H. Surface enhanced raman spectroscopy of lactoferrin adsorbed on silvered porous silicon covered with graphene. *Biosensors*, **2019**, *9,* 34.
37. Cançado, L.; Takai, K.; Enoki, T.; Endo, M.; Kim, Y.A.; Mizusaki, H.; Jorio, A.; Coelho, L. N.; Magalhães-Paniago, R.; Pimenta, M. A. General equation for the determination of the crystallite size La of nanographite by Raman spectroscopy. *Appl. Phys. Lett.*, **2006**, *88*, 163106.
38. Ferreira, E. H. M.; Moutinho, M. V. O.; Stavale, F.; Lucchese, M. M.; Capaz, R. B.; Achete, C. A.; Jorio, A. Evolution of the Raman spectra from single-, few-, and many-layer graphene with increasing disorder. *Phys. Rev. B*, **2010**, *82*, 125429.
39. Ferrari, A. C.; Robertson, J. Interpretation of Raman spectra of disordered and amorphous carbon. *Phys. Rev. B*, **2000**, *61*, 14095-14107.
40. Ferrari, A. C. Raman spectroscopy of graphene and graphite: Disorder, electron-phonon coupling, doping and nonadiabatic effects. *Solid State Commun*., **2007**, *143*, 47-57.
41. Nakamoto, K. Infrared and Raman spectra of inorganic and coordination compounds. 4th Ed. John Wiley & Sons, 1984, p. 484.

42. Khandelwal, M.; Kumar, A. One-step chemically controlled wet synthesis of graphene nanoribbons from graphene oxide for high performance supercapacitor applications. *J. Mater. Chem. A,* **2015**, *3*, 22975-22988.
43. Lia, Y.-S.; Church, J. S.; Woodhead, A. L. Infrared and Raman spectroscopic studies on iron oxide magnetic nano-particles and their surface modifications. J. *Magn. Magn. Mater*., **2012**, *324*, 1543-1550.
44. de Faria, D. L. A.; Silva, S. V.; de Oliveira, M. T.; Raman microspectroscopy of some iron oxides and oxyhydroxides. *J Raman Spectrosc*., **1997**, *28*, 873-878.
45. Trusovas, R.; Račiukaitis, G.; Niaura, G.; Barkauskas, J.; Valušis, G.; Pauliukaite, R. Recent advances in laser utilization in the chemical modification of graphene oxide and its Applications. *Adv. Optical Mater.*, **2016**, *4*, 37-65.
46. Soler, M. A. G.; Qu, F. Chapter 14: Raman spectroscopy of iron oxide nanoparticles. Challa S. S. R. Kumar (ed.), Raman spectroscopy for nanomaterials characterization, Springer-Verlag Berlin Heidelberg 2012, 379-416.
47. Perkins, R. S.; Garber, J. D. Raman spectroscopy of iron in aqueous carbonate solutions. *J Sol. Chem.*, **2003**, *32*, 265-272.
48. Ferrari, A. C.; Robertson, J. Origin of the 1150 cm^{-1} Raman mode in nanocrystalline diamond. *Phys. Rev. B*, **2001**, *63*, 121405-1-4.
49. Díez-Betriu, X.; Álvarez-García, S.; Botas, C.; Álvarez, P.; Sánchez-Marcos, J.; Prieto, C.; Menéndez, R.; de Andrés, A. Raman spectroscopy for the study of reduction mechanisms and optimization of conductivity in graphene oxide thin films. *J. Mater. Chem. C*, **2013**, *1*, 6905-6912.
50. Wang, Y.; Alsmeyer, D. C.; McCreery, R. L. Raman spectroscopy of carbon materials: structural basis of observed spectra. *Chem. Mater*., **1990**, *2*, 557-563.
51. Loh, K. P.; Bao, Q.; Eda, G.; Chhowalla, M. Graphene oxide as a chemically tunable platform for optical applications. *Nat. Chem.*, **2010**, *2*, 1015-1024.
52. Guo, P.; Song, H.; Chen, X. Hollow graphene oxide spheres self-assembled by W/O emulsion. *J. Mater. Chem*., **2010**, *20*, 4867-4874.
53. Krishnamoorthy, K.; Veerapandian, M.; Yun, K.; Kim, S.-J. The chemical and structural analysis of graphene oxide with different degrees of oxidation. *Carbon*, **2013**, *53*, 38-49.
54. Suslick, K. S.; Hammerton, D. A.; Cline, R. E. The sonochemical hot spot. *J. Am. Chem. Soc.*, **1986**, *108*, 5641-5642.
55. Lavina, B.; Dera, P.; Kim, E.; Meng, Y.; Downs, R. T.; Weck, P. F.; Sutton, S. R.; Zhao, Y. Discovery of the recoverable high-pressure iron oxide Fe_4O_5. *PNAS*, **2011**, *108*, 17281-17285.

56. Tang, L.; Ji, R.; Cao, X.; Lin, J.; Jiang, H.; Li, X.; Teng, K. S.; Luk, C. M.; Zeng, S.; Hao, J.; Lau, S. P. Deep ultraviolet photoluminescence of water-soluble self-passivated graphene quantum dots. *ACS Nano*, **2012**, *6*, 5102-5110.
57. Liang, Y.; Wu, D.; Feng, X.; Müllen, K. Dispersion of graphene sheets in organic solvent supported by ionic interactions. *Adv. Mater.*, **2009**, *21*, 1679-1683.
58. He, Y. P.; Miao, Y. M.; Li, C. R.; Wang, S. Q.; Cao, L.; Xie, S. S.; Yang, G. Z.; Zou, B. S.; Burda, C. Size and structure effect on optical transitions of iron oxide nanocrystals. *Phys. Rev. B*, **2005**, *71*, 125411.
59. Rainsford, K. D. Aspirin and related drugs, CRC Press Inc., UK, 2004, p. 800.
60. Lai, Q.; Zhu, S.; Luo, X.; Zou, M.; Huang, S. Ultraviolet-visible spectroscopy of graphene oxides. *AIP Advances*, **2012**, *2*, 032146.
61. Robinson, J. W. Practical handbook of spectroscopy, Section 7, p. 578, CRC Press Inc., UK, 1991.
62. Tang, J.; Myers, M.; Bosnick, K. A.; Brus, L. E. Magnetite Fe_3O_4 nanocrystals: spectroscopic observation of aqueous oxidation kinetics. *J. Phys. Chem. B*, **2003**, *107*, 7501-7506.
63. Brela, M. Z.; Wójcik, M. J.; Witek, Ł. J.; Boczar, M.; Wrona, E.; Hashim, R.; Ozaki, Y. Born–Oppenheimer molecular dynamics study on proton dynamics of strong hydrogen bonds in aspirin crystals, with emphasis on differences between two crystal forms. *J Phys. Chem. B*, **2016**, *120*, 3854-3862.
64. Berg, R. W. Investigation of L(+)-ascorbic acid with Raman spectroscopy in visible and UV light. *Appl. Spectrosc. Rev*., **2015**, *50*, 193-239.
65. Boczar, M.; Wójcik, M. J.; Szczeponek, K.; Jamróz, D.; Zięba, A.; Kawałek, B. Theoretical modeling of infrared spectra of aspirin and its deuterated derivative. *Chem. Phys*., **2003**, *286*, 63-79.
66. Cooney, T. F.; Wang, L.; Sharma, S. K.; Gauldie, R. W.; Montana, A. J. Raman spectral study of solid and dissolved poly(vinyl alcohol) and ethylene-vinyl alcohol copolymer. *J Polym. Sci.: Part B: Polym. Phys*., **1994**, *32*, 1163-1174.

Table of Contents Graphic

Coating of ultrasonically formed acetylsalicylic acid-Fe_3O_4-graphene oxide nanocomposites with polyvinyl alcohol substantially enhances acetylation of pristine ascorbic acid.